Floquet topological semimetal with a helical nodal line in 2+1 dimensions

Kun Woo Kim,[1] Hyunwoong Kwon,[2] and Kwon Park[1,2,*]
[1]*School of Physics, Korea Institute for Advanced Study, Seoul 02455, Korea*
[2]*Quantum Universe Center, Korea Institute for Advanced Study, Seoul 02455, Korea*

(Received 21 November 2018; published 25 March 2019)

Topological semimetals with a nodal line is a class of topological matter extending the concept of topological matter beyond topological insulators and Weyl/Dirac semimetals. Here we show theoretically that a Floquet topological semimetal with a helical nodal line can be generated in 2+1 dimensions by irradiating graphene or the surface of a topological insulator with circularly polarized light. The helical nodal line is the nodal line running across the Brillouin zone with helical winding. Specifically, it is shown that the dynamics of irradiated graphene is described by the time Stark Hamiltonian, which can host a Floquet topological insulator and a weakly driven Floquet topological semimetal with a helical nodal line in the high and low frequency limits, respectively. One of the most striking features of the Floquet topological semimetal at low frequency is that the Berry phase accumulated along the time direction, also known as the Zak phase, has a topological discontinuity of π across the projected helical nodal line. It is predicted that such a topological discontinuity of the Berry phase manifests itself as the topological discontinuity of the Floquet states. At intermediate frequency, this topological discontinuity can create an interesting change of patterns in the quasienergy dispersion of the Floquet states.

DOI: 10.1103/PhysRevB.99.115136

I. INTRODUCTION

Topological matter can be classified in various ways. An intuitive way is to note how Dirac monopoles are located in the Hamiltonian parameter space. In the case of topological insulators [1–5], Dirac monopoles exist in an appropriate, but hidden parameter space, while avoided in the momentum space [6]. In the case of Weyl [7,8] and Dirac [9] semimetals, they are directly located in the momentum space as isolated points. Topological semimetals with a nodal line [10] can be regarded as a class of topological matter where Dirac monopoles form a closed loop in the momentum space. Despite considerable attention, however, conclusive experimental evidence for the topological semimetals with a nodal line has been elusive so far, partly since they require a rather delicate symmetry protection in real materials [11–22].

Meanwhile, there has been a rapidly growing interest in the artificial generation of topological matter in time-dependent periodic systems, dubbed Floquet engineering [23]. One of the most notable examples is the theoretical proposal for the generation of a Floquet topological insulator by irradiating graphene [24–29] or semiconductor quantum wells [30]. The Floquet topological insulator generated in the high frequency limit of irradiated graphene is particularly interesting since it can provide an exact realization of the Haldane model [1] or the Kane-Mele model [2] for a single spin species with the possibility of manipulating the Chern number via tuning the radiation frequency and electric field strength.

Here we show that, in addition to the Floquet topological insulator in the high frequency limit, irradiated graphene can host a weakly driven Floquet topological semimetal with a helical nodal line at low frequency, which resides in 2+1 dimensions with one additional dimension being the time. With the helical nodal line being the nodal line running across the time Brillouin zone [18], this provides a platform for the artificial generation of topological semimetals with a nodal line. A salient feature of the so-obtained Floquet topological semimetal is the π shift of the Zak phase inside the projected helical nodal line, giving rise to the topological discontinuity across the projected helical nodal line in the momentum spectrum of the Floquet states. At intermediate frequency, this topological discontinuity can create an interesting change of patterns in the quasienergy dispersion of the Floquet states, which cannot be understood in terms of the simple overlapping Floquet copies of the Dirac dispersion. Having the same dispersion as graphene in the continuum limit, the surface of a topological insulator can also serve as another promising platform for the Floquet topological semimetal with a helical nodal line in 2+1 dimensions. We discuss the feasibility of its experimental observation via time- and angle-resolved photoemission spectroscopy (TARPES) [31,32].

II. TIME STARK HAMILTONIAN

When the Hamiltonian $\hat{H}(t)$ is periodic in time with period $T = 2\pi/\Omega$, the Floquet theorem dictates that the solution of the Schrödinger equation is generally written as $|\Psi_\alpha(t)\rangle = e^{-i\epsilon_\alpha t/\hbar}|\psi_\alpha(t)\rangle$ with $|\psi_\alpha(t)\rangle$ being a periodic function of time with the same period, i.e., $|\psi_\alpha(t)\rangle = \sum_n e^{-in\Omega t}|\psi_\alpha^n\rangle$, where n is the Fourier index. The quasienergy eigenvalue ϵ_α and the Fourier components $\{|\psi_\alpha^n\rangle\}$ of the αth Floquet state can be determined by diagonalizing the Floquet Hamiltonian:

$$[\hat{H}_F]_{nm} = \hat{H}_{nm} - n\hbar\Omega\delta_{nm}, \quad (1)$$

*kpark@kias.re.kr

where $\hat{H}_{nm} = \frac{1}{T}\int_0^T \hat{H}(t)e^{i(n-m)\Omega t}dt$. We set $\hbar = 1$ from here forward.

The Floquet Hamiltonian can be interpreted as the Fourier-transformed Stark Hamiltonian, where an effective dc electric field with the strength Ω is represented via the corresponding effective electrostatic potential in the Fourier space [33]. In this paper, we show that a unified understanding of the Floquet dynamics in the two opposite limits of high and low frequencies can be achieved by analyzing the Stark Hamiltonian expressed directly in terms of time, which we call the time Stark Hamiltonian (TSH):

$$\hat{H}_{\rm TS}(\mathbf{k}) = \hat{\mathcal{E}}(\mathbf{k}) + \Omega\left[i\frac{\partial}{\partial\kappa} + \hat{\mathcal{A}}_\kappa(\mathbf{k})\right], \tag{2}$$

where $\mathbf{k} = (\mathbf{k}_\perp, \kappa)$ is the extended momentum with two real, $\mathbf{k}_\perp = (k_x, k_y)$, and one effective, $\kappa = -\Omega t$, momentum components. Note that, here, we are interested in the time-dependent periodic systems in two spatial dimensions. Also, note that, for convenience, we have chosen κ to be negatively proportional to time so that the quasienergy increases in magnitude along the effective electric field direction. $\hat{\mathcal{E}}(\mathbf{k})$ is the *instantaneous* energy eigenvalue matrix obtained by diagonalizing the nominal Hamiltonian, $\hat{H}(\mathbf{k})$, which is simply the original Hamiltonian with Ωt just replaced by $-\kappa$. Mathematically, $[\hat{\mathcal{E}}(\mathbf{k})]_{ab} = \epsilon_a(\mathbf{k})\delta_{ab}$ with $\epsilon_a(\mathbf{k})$ being the instantaneous eigenvalue of $\hat{H}(\mathbf{k})$ for the ath band. $\hat{\mathcal{A}}_\kappa(\mathbf{k})$ is the non-Abelian Berry connection projected along the κ direction; $[\hat{\mathcal{A}}_\kappa(\mathbf{k})]_{ab} \equiv \mathcal{A}_\kappa^{ab}(\mathbf{k}) = \langle u_a(\mathbf{k})|i\frac{\partial}{\partial\kappa}|u_b(\mathbf{k})\rangle$ with $|u_a(\mathbf{k})\rangle$ and $|u_b(\mathbf{k})\rangle$ being the instantaneous eigenstates of $\hat{H}(\mathbf{k})$ for the ath and bth bands, respectively. See Appendix A for the detailed derivation of the TSH. It is interesting to note that essentially the same Hamiltonian has been studied in the context of topological insulators [34] and Weyl semimetals [35] under a real dc electric field.

To be specific, the graphene Hamiltonian without radiation can be written as follows:

$$\hat{H}_0(\mathbf{k}_\perp) = \begin{pmatrix} 0 & g_{\mathbf{k}_\perp} \\ g^*_{\mathbf{k}_\perp} & 0 \end{pmatrix}, \tag{3}$$

where $g_{\mathbf{k}_\perp} = -\tau(e^{i\mathbf{k}_\perp\cdot\mathbf{c}_1} + e^{i\mathbf{k}_\perp\cdot\mathbf{c}_2} + e^{i\mathbf{k}_\perp\cdot\mathbf{c}_3})$ with $\mathbf{c}_1 = (-\sqrt{3}/2, -1/2)$, $\mathbf{c}_2 = (\sqrt{3}/2, -1/2)$, and $\mathbf{c}_3 = (0, 1)$ in units of lattice spacing, which is set to be unity throughout this paper. τ is the hopping parameter between nearest-neighboring sites. The Hamiltonian in the presence of circularly polarized radiation can be obtained via Peierls substitution, $\mathbf{k}_\perp \to \mathbf{k}_\perp^{\rm Pei\text{-}sub} = \mathbf{k}_\perp - \frac{e}{c}\mathbf{A}(t)$, where the vector potential is $\mathbf{A}(t) = \frac{cE_0}{\Omega}(\cos\Omega t, -\sin\Omega t)$ with E_0 being the radiation electric field strength. In the extended momentum notation, $\mathbf{k}_\perp^{\rm Pei\text{-}sub} = (k_x - A\cos\kappa, k_y - A\sin\kappa)$ with $A = eE_0/\Omega$. In summary, the graphene Hamiltonian in the presence of circularly polarized radiation is written in the extended momentum notation as follows:

$$\hat{H}(\mathbf{k}) = \begin{pmatrix} 0 & g_{\mathbf{k}} \\ g^*_{\mathbf{k}} & 0 \end{pmatrix}, \tag{4}$$

where $g_{\mathbf{k}} = g_{\mathbf{k}_\perp^{\rm Pei\text{-}sub}}$.

The instantaneous eigenstates of $\hat{H}(\mathbf{k})$ in Eq. (4) are given by

$$|u_\pm(\mathbf{k})\rangle = \frac{1}{\sqrt{2}}\begin{pmatrix} e^{-i\phi(\mathbf{k})} \\ \pm 1 \end{pmatrix}, \tag{5}$$

where $e^{-i\phi(\mathbf{k})} = g_{\mathbf{k}}/|g_{\mathbf{k}}|$. The corresponding instantaneous eigenvalues are $\epsilon_\pm(\mathbf{k}) = \pm|g_{\mathbf{k}}|$, where $\pm$ indicates the conduction and valence bands, respectively. Consequently, the instantaneous energy eigenvalue matrix in Eq. (2) is given as

$$\hat{\mathcal{E}}(\mathbf{k}) = \begin{pmatrix} |g_{\mathbf{k}}| & 0 \\ 0 & -|g_{\mathbf{k}}| \end{pmatrix}, \tag{6}$$

indicating that the energy gap closes when $|g_{\mathbf{k}}| = 0$. Visually, each Dirac node spirals around its original position, forming a helical nodal line with radius A. Meanwhile, the instantaneous eigenstates give rise to the following Berry connection:

$$\hat{\mathcal{A}}_\kappa(\mathbf{k}) = \frac{1}{2}\frac{\partial\phi(\mathbf{k})}{\partial\kappa}\begin{pmatrix} 1 & 1 \\ 1 & 1 \end{pmatrix}. \tag{7}$$

In conclusion, the dynamics of irradiated graphene is described by the TSH, where an effective dc electric field is applied along the axis of the helical nodal line. See Fig. 1 for illustration.

The TSH needs to be solved numerically at general frequencies. Fortunately, however, one can obtain quite useful analytical expressions for the two topologically interesting solutions in the limits of high and low frequencies, respectively. The main goal of this work is to investigate what happens in the limit of low frequency. Before elaborating on this, we show how the TSH can capture the emergence of a Floquet topological insulator in the limit of high frequency.

III. FLOQUET TOPOLOGICAL INSULATOR AT HIGH FREQUENCY

It is well known that a Floquet topological insulator can emerge in irradiated graphene with circularly polarized light at high frequency [24–29,36]. A question is how the TSH in Eq. (2) can capture this.

In the limit of high frequency, one can proceed by first solving the second term in Eq. (2), which has Ω as a prefactor,

$$H_\Omega = \Omega\left[i\frac{\partial}{\partial\kappa} + \frac{1}{2}\frac{\partial\phi(\mathbf{k})}{\partial\kappa}\begin{pmatrix} 1 & 1 \\ 1 & 1 \end{pmatrix}\right], \tag{8}$$

and then taking into account the first term, $\hat{\mathcal{E}}$. H_Ω can be diagonalized analytically via the following eigenstates with the corresponding eigenvalue ν:

$$|\varphi_{\pm,\nu}(\mathbf{k})\rangle = \frac{1}{\sqrt{2}}\begin{pmatrix} 1 \\ \pm 1 \end{pmatrix} f_{\pm,\nu}(\mathbf{k}), \tag{9}$$

where $f_{+,\nu}(\mathbf{k}) = e^{-i[\nu\kappa - \Delta\phi(\mathbf{k})]}$ and $f_{-,\nu}(\mathbf{k}) = e^{-i\nu\kappa}$ with $\Delta\phi(\mathbf{k}) = \phi(\mathbf{k}_\perp, \kappa) - \phi(\mathbf{k}_\perp, 0)$. Due to the periodic boundary condition, ν is an integer. Let us call $|\varphi_{\pm,\nu}(\mathbf{k})\rangle$ the high-frequency eigenstate from this forward.

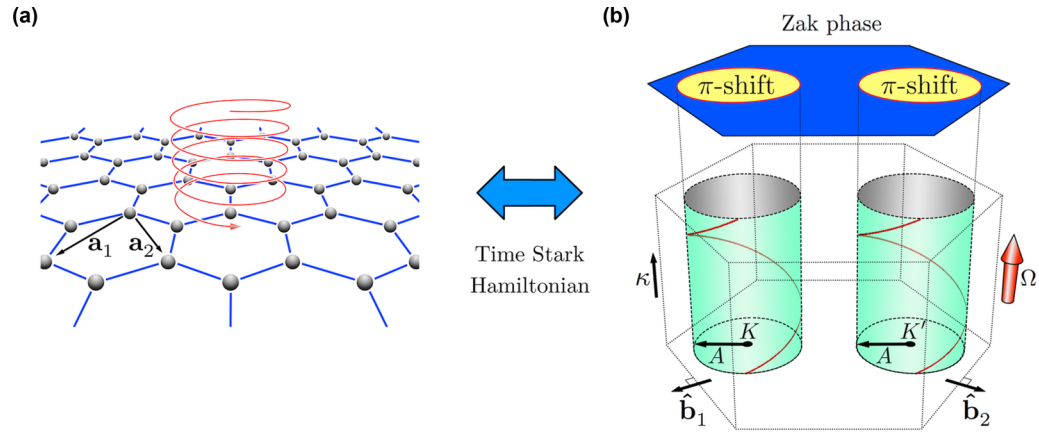

FIG. 1. Schematic diagram showing the mapping of irradiated graphene from the real (a) to the extended momentum (b) space. Here, $\mathbf{a}_1$ and $\mathbf{a}_2$ denote the primitive lattice vectors of graphene in the real space, while $\hat{\mathbf{b}}_1$ and $\hat{\mathbf{b}}_2$ denote the unit reciprocal lattice vectors in the extended momentum space. The dynamics of irradiated graphene is described by the time Stark Hamiltonian in the extended momentum space, where an effective dc electric field with the strength equal to the radiation frequency Ω is applied along the axis of the helical nodal line aligned with the time, i.e., $\kappa = -\Omega t$ direction. Note that the helical nodal line is the trajectory of each Dirac node encircling either K or K' as a function of time. The radius of the helical nodal line is given by $A = eE_0/\Omega$ with E_0 being the radiation electric field strength. The Zak phase accumulated along the κ direction acquires a relative π shift inside the projected helical nodal line due to the same reason why the Su-Schrieffer-Heeger model becomes topological. At low frequency, the π shift of the Zak phase gives rise to the topological discontinuity across the projected helical nodal line in the momentum spectrum of the Floquet states.

By using the high-frequency eigenstates as a new basis set, one can reexpress $\hat{\mathcal{E}}$ in the following matrix form:

$$\mathcal{M}_{\hat{\mathcal{E}}} = \begin{pmatrix} \ddots & \ddots & \ddots & & \\ \ddots & \hat{\Gamma}_0 & \hat{\Gamma}_1^\dagger & \hat{\Gamma}_2^\dagger & \\ \ddots & \hat{\Gamma}_1 & \hat{\Gamma}_0 & \hat{\Gamma}_1^\dagger & \ddots \\ & \hat{\Gamma}_2 & \hat{\Gamma}_1 & \hat{\Gamma}_0 & \ddots \\ & & \ddots & \ddots & \ddots \end{pmatrix}, \tag{10}$$

where

$$\hat{\Gamma}_n = \begin{pmatrix} 0 & \Gamma_n(\mathbf{k}_\perp) \\ \Gamma^*_{-n}(\mathbf{k}_\perp) & 0 \end{pmatrix}, \tag{11}$$

and $\Gamma_n(\mathbf{k}_\perp) = e^{i\phi_0(\mathbf{k}_\perp)} \int_0^{2\pi} \frac{d\kappa}{2\pi} g_{\mathbf{k}} e^{in\kappa}$ with $\phi_0(\mathbf{k}_\perp) = \phi(\mathbf{k}_\perp, \kappa = 0)$. The entire TSH including both terms in Eq. (2) can be written as $\mathcal{H}_{\rm TS} = \mathcal{M}_{\hat{\mathcal{E}}} + \mathcal{M}_\Omega$, where $\mathcal{M}_\Omega$ is the diagonal matrix with $[\mathcal{M}_\Omega]_{\nu\nu'} = \nu\Omega\hat{I}\delta_{\nu\nu'}$ for the (ν, ν')-th 2×2 block.

Now, $\mathcal{H}_{\rm TS}$ can be systematically expanded as a power series of $1/\Omega$. Specifically, valid up to the order of $1/\Omega$, the following effective 2×2 Hamiltonian can be obtained for the νth pair of the quasienergy bands:

$$\mathcal{H}_{{\rm eff},\nu} = \begin{pmatrix} \nu\Omega & \Gamma_0 \\ \Gamma_0^* & \nu\Omega \end{pmatrix} + \sum_{n=1}^{\infty} \frac{|\Gamma_n|^2 - |\Gamma_{-n}|^2}{n\Omega} \begin{pmatrix} 1 & 0 \\ 0 & -1 \end{pmatrix}. \tag{12}$$

Note that the above effective Hamiltonian can be derived by combining the degenerate perturbation theory for the effects of Γ_0 within the 2×2 diagonal block and the second-order perturbation theory for the virtual process mixing different blocks via $\Gamma_{n\neq 0}$.

After performing a series of integrations and algebras, one can show that, in the limit of high frequency, $\mathcal{H}_{{\rm eff},\nu}$ can be rewritten as follows:

$$\mathcal{H}_{{\rm eff},\nu} = \nu\Omega\hat{I} + \mathbf{d}_{\mathbf{k}_\perp} \cdot \boldsymbol{\sigma}, \tag{13}$$

where $d^*_{\mathbf{k}_\perp,+} = d_{\mathbf{k}_\perp,-} = -\tau_{\rm eff}(A) e^{i\phi_0(\mathbf{k}_\perp)} \sum_{j=1}^{3} e^{i\mathbf{k}_\perp \cdot \mathbf{c}_j}$ with $d_{\mathbf{k}_\perp,\pm} = d_{\mathbf{k}_\perp,x} \pm i d_{\mathbf{k}_\perp,y}$, and $d_{\mathbf{k}_\perp,z} = i\lambda_{\rm eff}(A) \sum_{j=1}^{6} (-1)^j e^{i\mathbf{k}_\perp \cdot \boldsymbol{\eta}_j}$ with $\boldsymbol{\eta}_j$ being the displacement vectors connecting between next-nearest-neighboring sites: $\boldsymbol{\eta}_1 = (-\sqrt{3}/2, -3/2)$, $\boldsymbol{\eta}_2 = (\sqrt{3}/2, -3/2)$, $\boldsymbol{\eta}_3 = (\sqrt{3}, 0)$, $\boldsymbol{\eta}_4 = (\sqrt{3}/2, 3/2)$, $\boldsymbol{\eta}_5 = (-\sqrt{3}/2, 3/2)$, and $\boldsymbol{\eta}_6 = (-\sqrt{3}, 0)$. The effective hopping and spin-orbit coupling parameters are given as $\tau_{\rm eff}(A) = \tau J_0(A)$ and $\lambda_{\rm eff}(A) = \frac{2\tau^2}{\Omega} \sum_{n=1}^{\infty} \frac{J_n^2(A)}{n} \sin(\frac{2n\pi}{3})$, respectively. It is important to note that these formulas are exactly the same as those previously obtained by using the degenerate perturbation theory [36] and the Brillouin-Wigner theory [29]. See Appendix B for the details of the derivation.

In summary, up to the order of $1/\Omega$ in the limit of high frequency, the TSH can be decomposed into an infinite ladder of the effective 2×2 Hamiltonians, $\mathcal{H}_{{\rm eff},\nu}$, each of which is exactly identical to the Kane-Mele model Hamiltonian [2] of a single spin species with the effective hopping parameter $\tau_{\rm eff}(A)$ and the effective spin-orbit coupling parameter $\lambda_{\rm eff}(A)$. Since the Kane-Mele model is nothing but two copies of the Haldane model with opposite flux configurations for different spin species, this means that $\mathcal{H}_{{\rm eff},\nu}$ is also exactly identical to the Haldane model Hamiltonian [1] describing a Chern insulator. It is interesting to mention that there has been a recent experimental paper reporting the observation of an anomalous Hall effect in irradiated graphene with a midinfrared femtosecond pulse of circularly polarized light [37].

Finally, it is important to note that the TSH can be expanded systematically beyond the first order of $1/\Omega$ in terms of the high-frequency eigenstate basis. Specifically, a systematic high-frequency expansion can be constructed essentially in the same way as the aforementioned degenerate perturbation and Brillouin-Wigner theories. Note that there are various other equivalent high-frequency expansion theories [38–40]. The detailed derivation of our systematic high-frequency expansion theory is to be published in a future paper.

Instead of providing such details here, we would like to focus on one of the most important properties of our high-frequency expansion theory, which is crucial for proving the equivalence between ours and various other theories. That is, the high-frequency eigenstate in our theory is in fact exactly identical to the usual Floquet-Bloch state used, for example, in the degenerate perturbation and Brillouin-Wigner theories. To show this, let us rewrite the high-frequency eigenstates $|\varphi_{\pm,\nu}(\mathbf{k})\rangle$ in terms of the instantaneous eigenstates $|u_{\pm}(\mathbf{k})\rangle$ by using the bra-ket notation,

$$|\varphi_{\pm,\nu}(\mathbf{k})\rangle = \frac{1}{\sqrt{2}} f_{\pm,\nu}(\mathbf{k})(|u_{+}(\mathbf{k})\rangle \pm |u_{-}(\mathbf{k})\rangle), \tag{14}$$

which is simply equal to Eq. (9). Similarly, according to Eq. (5), the instantaneous eigenstates can be written in terms of the Bloch states in 2+1 dimensions as follows:

$$|u_{\pm}(\mathbf{k})\rangle = \frac{1}{\sqrt{2}}(e^{-i\phi(\mathbf{k})}|A(\mathbf{k})\rangle \pm |B(\mathbf{k})\rangle), \tag{15}$$

where $|A(\mathbf{k})\rangle$ and $|B(\mathbf{k})\rangle$ denote the Bloch states for the A and B sublattices, respectively. By combining Eqs. (14) and (15), the high-frequency eigenstates can be written as follows:

$$|\varphi_{+,\nu}(\mathbf{k})\rangle = e^{-i\nu\kappa} e^{-i\phi_0(\mathbf{k}_\perp)}|A(\mathbf{k})\rangle, \tag{16}$$

$$|\varphi_{-,\nu}(\mathbf{k})\rangle = e^{-i\nu\kappa}|B(\mathbf{k})\rangle, \tag{17}$$

which means that the high-frequency eigenstates are nothing but the Floquet-Bloch states. Note that the phase factor $e^{-i\phi_0(\mathbf{k}_\perp)}$ is not important since it can be removed via an appropriate gauge transformation.

IV. FLOQUET TOPOLOGICAL SEMIMETAL WITH HELICAL NODAL LINE AT LOW FREQUENCY

The low frequency limit of the TSH is particularly interesting in the context of topological semimetals with a nodal line. In the limit of low frequency, the band-mixing terms, i.e., the off-diagonal elements of the non-Abelian Berry connection can be ignored. In other words, one can take the adiabatic approximation, where the Berry connection can be approximated to be Abelian by keeping only the diagonal terms. This can be done since the off-diagonal band-mixing terms are proportional to the driving frequency, while the diagonal terms have both kinetic energy and diagonal Berry connection terms. A zeroth-order approximation for the low-frequency limit would be to ignore all the terms proportional to the driving frequency, which means dropping all the Berry connection terms. However, this approximation would be too crude. A better approximation is to ignore the off-diagonal band-mixing terms while only keeping the diagonal Berry connection terms, which affects the quasienergy by adding corrections to the band dispersion.

The eigenstates of the Abelian Stark Hamiltonian under a dc electric field are known as the WSL eigenstates. By analogy, let us call the eigenstates of the Abelian TSH the time WSL eigenstates. The Abelian TSH for the ath band can be written as

$$\hat{H}_{\mathrm{ATS},a} = \epsilon_a(\mathbf{k}) + \Omega\left(i\frac{\partial}{\partial\kappa} + \mathcal{A}^{aa}_{\kappa}(\mathbf{k})\right), \tag{18}$$

which can, in turn, be diagonalized by the following time WSL eigenstates:

$$\psi^{\mathrm{WSL}}_{a,n}(\mathbf{k}) = e^{-\frac{i}{\Omega}\int_0^{\kappa} d\kappa' \left[\mathcal{E}^{\mathrm{WSL}}_{a,n}(\mathbf{k}_\perp) - \epsilon_a(\mathbf{k}') - \Omega\mathcal{A}^{aa}_{\kappa}(\mathbf{k}')\right]}, \tag{19}$$

where $\mathbf{k}' = (\mathbf{k}_\perp, \kappa')$. The above form of the time WSL eigenstates can be derived by noticing that the diagonalization of the Abelian TSH amounts to solving the following first-order differential equation:

$$\frac{\partial}{\partial\kappa}\psi^{\mathrm{WSL}}_{a}(\mathbf{k}) = -\frac{i}{\Omega}\left[\mathcal{E}_a(\mathbf{k}_\perp) - \epsilon_a(\mathbf{k}) - \mathcal{A}^{aa}_{\kappa}(\mathbf{k})\right]\psi^{\mathrm{WSL}}_{a}(\mathbf{k}), \tag{20}$$

where it is important to remember that the quasienergy $\mathcal{E}_a(\mathbf{k}_\perp)$ is independent of κ, while depending on the band index a. Note that the dependence of $\mathcal{E}_a(\mathbf{k}_\perp)$ and $\psi^{\mathrm{WSL}}_{a}(\mathbf{k})$ on the time WSL index n is introduced after the quantization of the quasienergy.

The quasienergy of the time WSL eigenstates is quantized via the periodic boundary condition, $\psi^{\mathrm{WSL}}_{a}(\mathbf{k}_\perp, \kappa + 2\pi) = \psi^{\mathrm{WSL}}_{a}(\mathbf{k}_\perp, \kappa)$. Specifically,

$$\mathcal{E}^{\mathrm{WSL}}_{a,n}(\mathbf{k}_\perp) = \bar{\epsilon}_a(\mathbf{k}_\perp) + \Omega\left(n + \frac{\gamma^{\mathrm{Zak}}_{a}(\mathbf{k}_\perp)}{2\pi}\right), \tag{21}$$

where the time WSL index n is an integer, $\bar{\epsilon}_a(\mathbf{k}_\perp) = \frac{1}{2\pi}\oint d\kappa \epsilon_a(\mathbf{k})$ is the time-averaged instantaneous band energy, and $\gamma^{\mathrm{Zak}}_{a}(\mathbf{k}_\perp) = \oint d\kappa \mathcal{A}^{aa}_{\kappa}(\mathbf{k})$ is the Zak phase accumulated along the κ direction. It is interesting to note that the importance of the geometric phase in the Floquet spectrum was previously pointed out in Ref. [24] by using the concept known as the Aharonov-Anandan phase, which can be applicable even in nonadiabatic situations. Also, there have been related theoretical studies showing the effect of the geometric phase in the real-time dynamics [41,42].

The time WSL eigenstates of irradiated graphene have an intriguing topological structure induced by the π shift of the Zak phase inside the projected helical nodal line. Mathematically, $\gamma^{\mathrm{Zak}}_{\pm}(\mathbf{k}_\perp) = \frac{1}{2}\oint d\kappa \frac{\partial}{\partial\kappa}\phi(\mathbf{k}) = \pi$ and 0 for $\mathbf{k}_\perp$ located inside and outside the projected helical nodal line, respectively. Intuitively, the π shift of the Zak phase can be understood as follows. With an addition of the circularly polarized radiation, each Dirac node performs a circular motion around either K or K' point as a function of time. As far as the acquired Berry, or Zak phase is concerned, however, there is no difference between this and the usual situation, where the momentum parameter of the Bloch state is adiabatically moved with a fixed Dirac node. This means that any Bloch state inside the trajectory of the circularly moving Dirac node acquires the π shift of the Berry phase, as if it would by encircling a fixed Dirac node. Mathematically, this is exactly the reason why the Su-Schrieffer-Heeger model becomes topological [43–46].

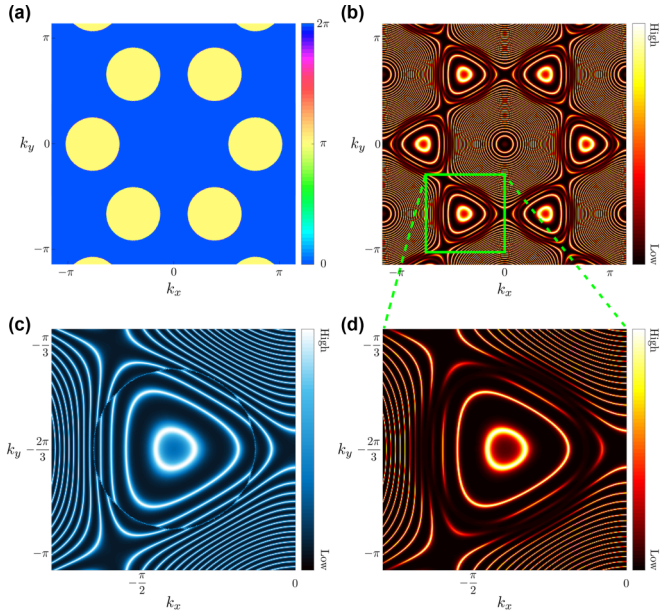

FIG. 2. Zero-energy momentum spectrum of the Floquet states in irradiated graphene at low frequency. Here, the radiation frequency is set to be $\Omega/\tau = 0.05$ with τ being the hopping parameter, and the radius of the helical nodal line is set to be $A = 0.8$. (a) Zak phase accumulated along the time direction, showing the π shift inside the projected helical nodal line. (b) Zero-energy momentum spectrum of the full Floquet states obtained by exactly solving either the Floquet or the time Stark Hamiltonian. (c) Closeup of the zero-energy momentum spectrum of the time Wannier-Stark ladder eigenstates obtained by solving the Abelian approximation of the time Stark Hamiltonian. (d) Closeup of the zero-energy momentum spectrum of the full Floquet states in the same region as (c), denoted by the green box in (b).

Consequently, the quasienergy of the time WSL eigenstates acquires the relative $\Omega/2$ shift inside the projected helical nodal line,

$$\mathcal{E}^{\rm WSL}_{\pm,n}(\mathbf{k}_\perp) = \begin{cases} \bar{\epsilon}_\pm(\mathbf{k}_\perp) + \Omega(n+1/2) & \text{(inside)} \\ \bar{\epsilon}_\pm(\mathbf{k}_\perp) + \Omega n & \text{(outside)}, \end{cases} \tag{22}$$

giving rise to the topological discontinuity across the projected helical nodal line.

Figure 2 shows the zero-energy momentum spectrum of the Floquet states in irradiated graphene at low frequency, showing the topological discontinuity across the projected helical nodal line. The zero-energy momentum spectrum of the full Floquet states can be obtained by exactly solving either the Floquet Hamiltonian or the TSH. Specifically, the quasienergy spectral function of the full Floquet states can be computed as

$$\rho(\omega, \mathbf{k}_\perp) = -\frac{1}{\pi}\mathrm{Im}\mathrm{Tr}\left[\frac{1}{\omega - \hat{H}_{\rm F} + i\eta}\right], \tag{23}$$

where $\hat{H}_{\rm F}$ is the Floquet matrix in Eq. (1) and the trace Tr is taken over both Floquet and sublattice indices. Then, the zero-energy momentum spectrum of the full Floquet states can be obtained by plotting $\rho(\omega = 0, \mathbf{k}_\perp)$ as a function of $\mathbf{k}_\perp$. Alternatively, one can just directly diagonalize the TSH by using the method developed in a previous work by some of the current authors [35].

Meanwhile, the zero-energy momentum spectrum of the time WSL eigenstates can be obtained by simply tracking all the $\mathbf{k}_\perp$ curves satisfying $\mathcal{E}^{\rm WSL}_{\pm,n}(\mathbf{k}_\perp) = 0$ for different n. A main message of Fig. 2 is that the zero-energy momentum spectrum of the full Floquet states is overall quite well captured by that of the time WSL eigenstates, providing a natural explanation for the existence of the topological discontinuity across the projected helical nodal line in terms of the π shift of the Zak phase.

Strictly speaking, however, the time WSL eigenstates is valid only in the limit of low frequency, where the Abelian approximation is applicable. Away from this limit, there is generally a mixing between different time WSL eigenstates from the conduction (+) and valence (−)bands. Note that there have been various theoretical efforts for the construction of a systematic perturbation theory beyond the adiabatic limit, taking the effects of the band-mixing terms into account [47–49].

Fortunately, in our system of interest, the effects of the band-mixing terms can be treated quite accurately without utilizing the full power of such a systematic perturbation theory. Specifically, it can be shown that the band-mixing terms generate the quasienergy gap of the Floquet states, which is highly localized near the projected helical nodal line without disturbing the overall structure of the momentum spectrum well captured by the time WSL eigenstates. Mathematically, the quasienergy gap near the projected helical nodal line can be computed quite accurately by using some form of the saddle point approximation. In particular, a quite accurate analytical formula can be obtained in the continuum limit, where the graphene Hamiltonian is taken to be linear in the vicinity of the Dirac node. Concretely, the quasienergy gap near the projected helical nodal line is given by

$$\mathcal{E}_{\rm gap} \simeq \frac{\Omega A}{\sqrt{2\pi\rho(A+\rho)}} e^{-\frac{2(A-\rho)^4}{\rho(A+\rho)(\Omega/\tau)^2}}, \tag{24}$$

where $\rho = |\mathbf{k}_\perp - \mathbf{K}_{\rm Dirac}|$ is the distance from the Dirac node. See Appendix C for the details of the derivation. It is important to note that the quasienergy gap vanishes much faster than Ω as soon as ρ becomes separated from A by roughly more than $\sqrt{A\Omega/\tau}$. This means that the topological discontinuity across the projected helical nodal line becomes more and more pronounced in the limit of low frequency.

Conversely speaking, away from the low frequency limit, the quasienergy gap is opened to smear out the topological discontinuity across the projected helical nodal line. The projected helical nodal line would appear as a *dark ring* with the width $\sqrt{A\Omega/\tau}$, which vanishes slower in the limit of low frequency than the separation distance between two adjacent time WSL eigenstates, Ω/τ. This means that the dark ring tracking the projected helical nodal line can be used as an experimental signature for the topological discontinuity since it may be easier to detect in the experimental situations, where the momentum resolution is not sufficient to distinguish between two adjacent Floquet states.

Figure 3 shows the comparison between the quasienergy dispersions of the time WSL eigenstates and the full Floquet states. It is important to note that the quasienergy gap is very

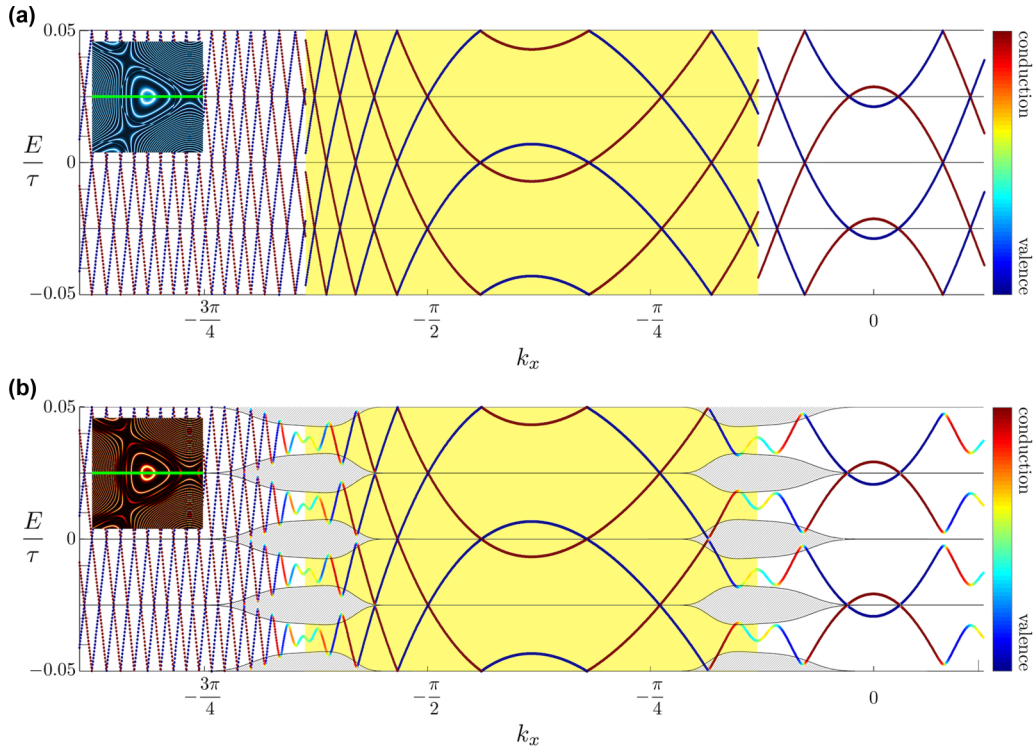

FIG. 3. Quasienergy dispersion of the Floquet states in irradiated graphene. Here, the radiation frequency and the radius of the helical nodal line are set to be the same corresponding values as Fig. 2. (a) Quasienergy dispersion of the time Wannier-Stark ladder eigenstates showing the mismatch of the quasienergy eigenvalues and hence the topological discontinuity at the projected helical nodal line. Note that the inside of the projected helical nodal line is denoted as a yellow region. (b) Quasienergy dispersion of the full Floquet states showing the opening of the quasienergy gap near the projected helical nodal line. The quasienergy gap is very well captured by the analytical formula $\mathcal{E}_{\text{gap}}$ in Eq. (24), the result of which is plotted as the shaded (grey) regions bounded by the thin black lines in the figure. Note that the thin black lines denote the plus and minus halves of $\mathcal{E}_{\text{gap}}$. Color indicates the Abelian weight measuring how much the Floquet states belongs to the conduction (red) or valence (blue) band. By construction, the time Wannier-Stark ladder (WSL) eigenstates belong to either one of the two bands exclusively. The green lines in the insets show the scanned momentum path, along which the quasienergy dispersion is computed.

well described by the analytical formula for $\mathcal{E}_{\text{gap}}$ in Eq. (24). This means that the full Floquet states are essentially given by the time WSL eigenstates except for the immediate vicinity of the projected helical nodal line. This fact is reaffirmed by the Abelian weight measuring how much the Floquet states belong to the conduction or valence band, or equivalently the overlap between the time WSL eigenstates and the full Floquet states. See Appendix D for the details on how to compute the Abelian weight.

Figure 4 shows the evolution of the Floquet states as a function of the radius of the helical nodal line. As one can see, the time WSL eigenstates can capture the evolution of the full Floquet states very well in a wide range of the radius of the helical nodal line. It is important to note that the momentum spectrum undergoes an interesting transition when the projected helical nodal lines overlap with those encircling different Dirac nodes.

V. FLOQUET STATES AT INTERMEDIATE FREQUENCY

Generally, the quasienergy dispersion is quite complicated at intermediate frequency. Nevertheless, the time WSL eigenstates can provide a useful guide to the full quasienergy dispersion.

For simplicity, let us take the continuum limit of graphene or the surface of a topological insulator under radiation, which has the same Hamiltonian expressed in the form of Eq. (4) with $g_{\mathbf{k}}$ replaced by $g_{\mathbf{q}} = \tau[(q_x - A\cos\kappa) + i(q_y - A\sin\kappa)]$ with $\mathbf{q} = (\mathbf{q}_\perp, \kappa)$ and $\mathbf{q}_\perp = (q_x, q_y) = \mathbf{k}_\perp - \mathbf{K}_{\text{Dirac}}$ being the momentum measured from the Dirac node. The quasienergy of the time WSL eigenstates in this limit can be obtained analytically via Eq. (22) with $\bar{\epsilon}_\pm(\mathbf{q}_\perp)$ given as follows:

$$\bar{\epsilon}_\pm(\mathbf{q}_\perp) = \pm\frac{2\tau A}{\pi}(1+r)E\left(\frac{2\sqrt{r}}{1+r}\right), \tag{25}$$

where $E(k)$ is the complete elliptic integral of the second kind and $r = \rho/A$ with $\rho = |\mathbf{q}_\perp|$. Considering the overall shape of the elliptic integral, the quasienergy dispersion of the time WSL eigenstates can be understood as being roughly quadratic and linear inside and outside the projected helical nodal line, respectively, with the relative topological shift by $\Omega/2$. Tuning the ratio between A and Ω/τ can create an interesting series of patterns in the quasienergy dispersion of the Floquet states.

Figure 5 shows the quasienergy dispersion of the Floquet states at an intermediate frequency with three representative ratios to the radius of the helical nodal line, say, $\Omega/\tau = 16A/\pi$, $8A/\pi$, and A. At $\Omega/\tau = 16A/\pi$, the

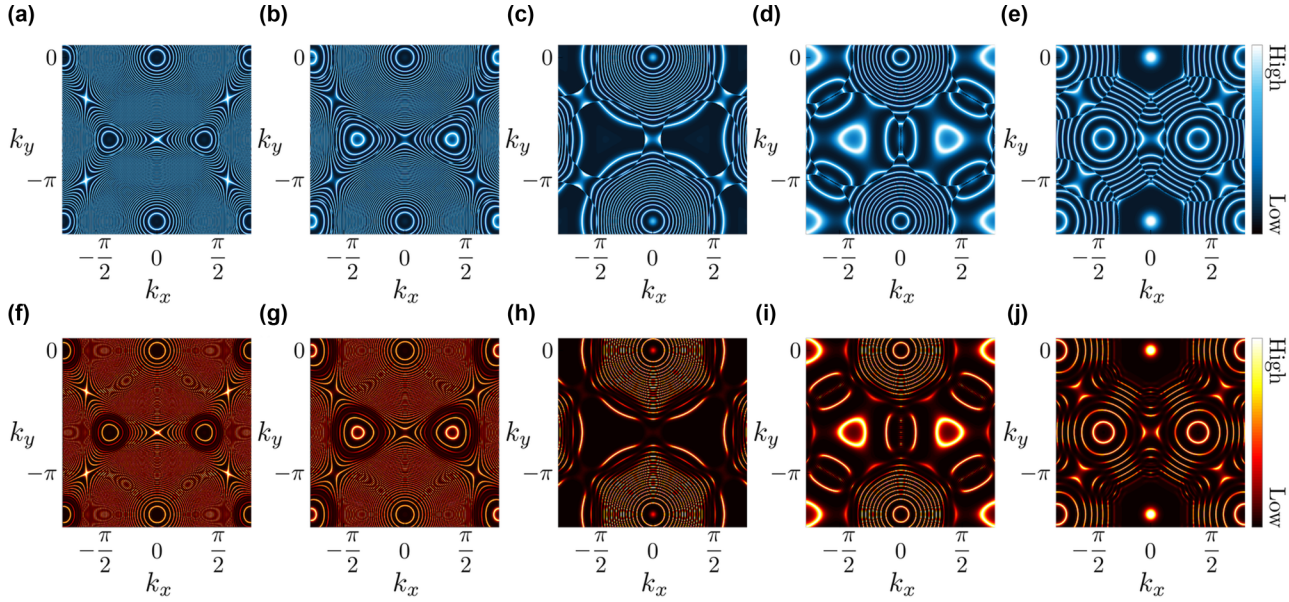

FIG. 4. Evolution of the Floquet states in irradiated graphene as a function of the radius of the helical nodal line. (a)–(e) Zero-energy momentum spectrum of the time Wannier-Stark ladder eigenstates. (f)–(j) Zero-energy momentum spectrum of the full Floquet states. Here, the radius of the helical nodal line A is changed from 0.4 [(a), (f)] to 0.6 [(b), (g)] to 1.0 [(c), (h)] to 1.2 [(d), (i)] to 1.6 [(e), (j)], while the radiation frequency Ω/τ is fixed as 0.05. Note that the projected helical nodal lines encircling different Dirac nodes are just about to touch at (d) and (i) and pass through each other at (e) and (j).

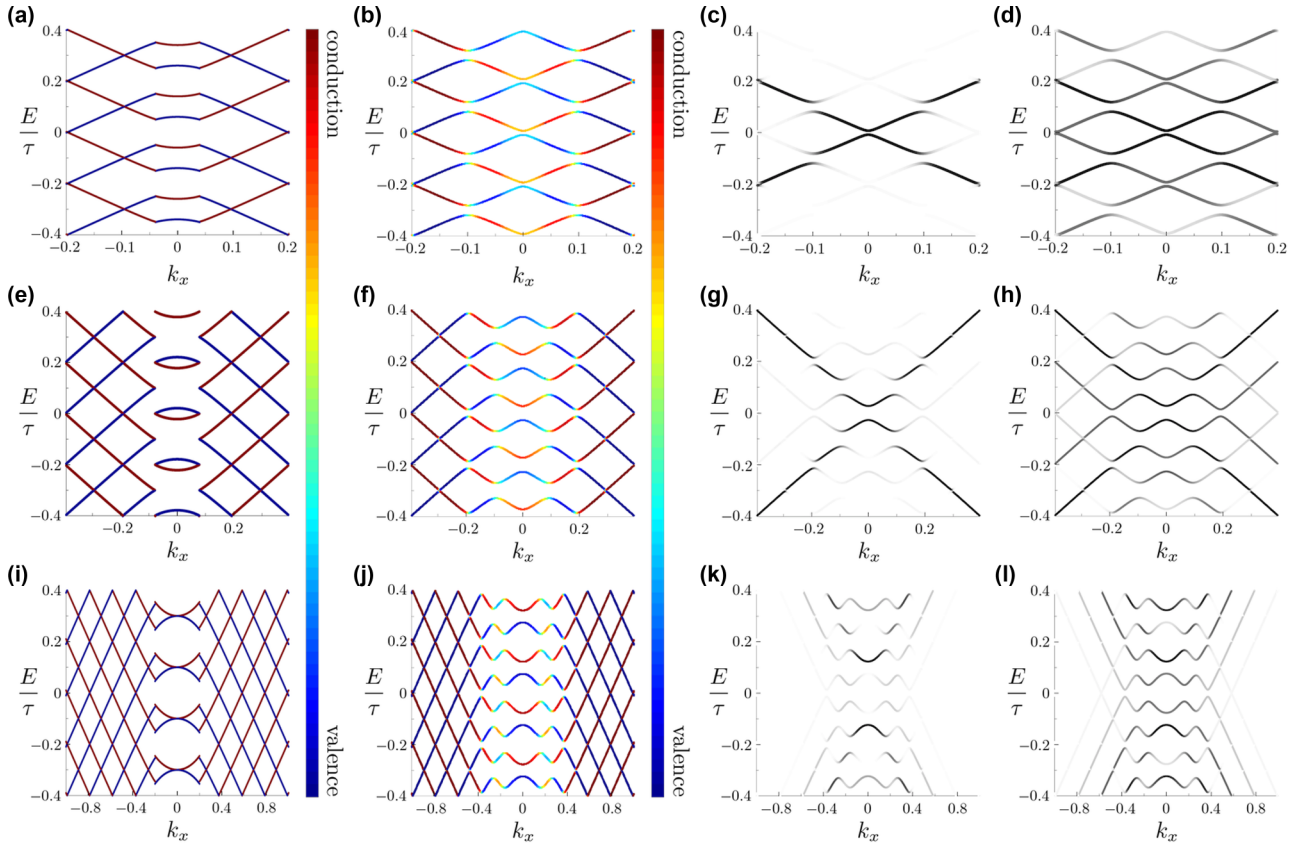

FIG. 5. Quasienergy dispersion of the Floquet states in the continuum limit at an intermediate frequency with three representative ratios to the radius of the helical nodal line. Specifically, $\Omega/\tau = 16A/\pi$ (a)–(d), $8A/\pi$ (e)–(h), and A (i)–(l) with $\Omega/\tau = 0.2$. (a), (e), (i) Quasienergy dispersion of the time Wannier-Stark ladder eigenstates. (b), (f), (j) Quasienergy dispersion of the full Floquet states. (c), (g), (k) Local density of Floquet states via the Gaussian probe weight with the standard deviation σ being $1/2$. (d), (h), (l) Local density of Floquet states via the Gaussian probe weight with the standard deviation σ being $3/2$. As one can see, at $\Omega/\tau = A$ (i)–(l), the quasienergy dispersion of the Floquet states cannot be understood in terms of the simple overlapping Floquet copies of the Dirac dispersion.

quasienergy dispersion can be rather well understood in terms of the simple overlapping Floquet copies of the Dirac dispersion with slight gap opening whenever different bands cross each other. Such a understanding is still possible at $\Omega/\tau = 8A/\pi$ despite some irregularities. At $\Omega/\tau = A$, however, it is no longer possible to do so. This change of patterns is due to the intricate interplay between the quasienergy dispersion inside and outside the projected helical nodal line having the relative topological shift by $\Omega/2$.

To compare with the actual experimental data obtained via TARPES, it is convenient to compute the "local density of Floquet states" (LDOFS), which is analogous to the local density of states under a dc electric field [34,35]. Mathematically, the LDOFS is defined as

$$\rho_{\rm loc}(\omega, \mathbf{k}_\perp) = \sum_{\alpha,n} \mathcal{W}_{\rm probe}(n) \langle \psi^n_{\alpha,\mathbf{k}_\perp} | \psi^n_{\alpha,\mathbf{k}_\perp} \rangle \delta(\omega - \epsilon_{\alpha,\mathbf{k}_\perp}), \tag{26}$$

where the "probe weight" $\mathcal{W}_{\rm probe}(n)$ is the Gaussian-like localized weight indicating the probability for an electron to exist in the nth Fourier component state after interacting with the probing light. For example, $\mathcal{W}_{\rm probe}(n) \propto e^{-(n-\bar{n})^2/2\sigma^2}$ with $\bar{n}$ and σ being the mean and the standard deviation, respectively. Note that $|\psi^n_{\alpha,\mathbf{k}_\perp}\rangle$ is the n-th Fourier component of the αth Floquet state at $\mathbf{k}_\perp$ with the quasienergy eigenvalue $\epsilon_{\alpha,\mathbf{k}_\perp}$. It is found that the quasienergy dispersion shown in the middle panels of Fig. 5 [specifically, Fig. 5(h)] is quite consistent with the experimental data obtained by Wang *et al.* via TARPES [31].

VI. DISCUSSION

In this paper, we have shown theoretically that a Floquet topological semimetal with a helical nodal line can be generated in 2+1 dimensions by irradiating graphene or the surface of a topological insulator with circularly polarized light. The dynamics of such a Floquet topological semimetal is described by the TSH, where an effective electric field is applied along the axis of the helical nodal line. In the case of irradiated graphene, the TSH can host a Floquet topological insulator and a weakly driven Floquet topological semimetal with a helical nodal line in the high and low frequency limits, respectively. Importantly, in the limit of low frequency, the π shift of the Zak phase inside the projected helical nodal line is predicted to generate the topological discontinuity across the projected helical nodal line in the momentum spectrum of the Floquet states. At intermediate frequency, this topological discontinuity can create an interesting change of patterns in the quasienergy dispersion of the Floquet states, which can be experimentally measured via TARPES.

We conclude this paper by discussing the possibility of observing the topological surface flat band [10], also known as the drumhead surface state, at the boundary of the Floquet lattice. Theoretically, the Floquet topological semimetal with a helical nodal line in 2+1 dimensions should have exactly the same topological surface flat band at the boundary as the usual topological semimetal with a nodal line in three dimensions. A question is what the boundary of the Floquet lattice means physically. The Floquet lattice site is labeled by the time-conjugate Fourier index denoting the nth harmonics of the driving frequency. We believe that the boundary of the Floquet lattice can be interpreted as the maximum or minimum cutoff harmonics, up to which electrons can respond to the driving electric field. If so, the topological surface flat band can be observed near this cutoff frequency.

ACKNOWLEDGMENTS

The authors are grateful to Sutirtha Mukherjee and Changsuk Noh for their insightful comments. The authors thank the KIAS Center for Advanced Computation (CAC) for providing computing resources. K.W.K. acknowledges support from Overseas Research Program for Young Scientists through Korea Institute for Advanced Study.

APPENDIX A: DERIVATION OF THE TIME STARK HAMILTONIAN

We begin by writing the time-periodic Schrödinger equation with $\hat{H}(\mathbf{k}_\perp, t+T) = \hat{H}(\mathbf{k}_\perp, t)$,

$$i\frac{\partial}{\partial t}|\Psi(\mathbf{k}_\perp, t)\rangle = \hat{H}(\mathbf{k}_\perp, t)|\Psi(\mathbf{k}_\perp, t)\rangle, \tag{A1}$$

where we set $\hbar = 1$ throughout this section. Note that, here, the dependence of the wave function on the real momentum $\mathbf{k}_\perp$ and time t are denoted separately. Now, according to the Floquet theorem, the wave function can be written as the product between the quasienergy phase factor and the time-periodic part,

$$|\Psi(\mathbf{k}_\perp, t)\rangle = e^{-i\epsilon t}|\psi(\mathbf{k}_\perp, t)\rangle, \tag{A2}$$

where $|\psi(\mathbf{k}_\perp, t+T)\rangle = |\psi(\mathbf{k}_\perp, t)\rangle$. Then, the time-periodic part of the wave function satisfies the following equation:

$$\left(i\frac{\partial}{\partial t} + \epsilon\right)|\psi(\mathbf{k}_\perp, t)\rangle = \hat{H}(\mathbf{k}_\perp, t)|\psi(\mathbf{k}_\perp, t)\rangle. \tag{A3}$$

In terms of the extended momentum notation $\mathbf{k} = (\mathbf{k}_\perp, \kappa)$ with $\kappa = -\Omega t$, the above equation can be rewritten as follows:

$$\epsilon|\psi(\mathbf{k})\rangle = \left(\hat{H}(\mathbf{k}) + i\Omega\frac{\partial}{\partial\kappa}\right)|\psi(\mathbf{k})\rangle, \tag{A4}$$

where it is important to note that t is guaranteed to appear in the form of Ωt due to the time-periodic property of $\hat{H}(\mathbf{k} = (\mathbf{k}_\perp, t))$ and $|\psi(\mathbf{k} = (\mathbf{k}_\perp, t))\rangle$.

Now, let us express the time-periodic part of the wave function in terms of the new basis set diagonalizing $\hat{H}(\mathbf{k})$. This new basis set is none other than the instantaneous eigenstate basis defined by the following unitary transformation:

$$\hat{\mathcal{U}}^\dagger(\mathbf{k})\hat{H}(\mathbf{k})\hat{\mathcal{U}}(\mathbf{k}) = \hat{\mathcal{E}}(\mathbf{k}), \tag{A5}$$

where $\hat{\mathcal{E}}(\mathbf{k})$ is the instantaneous energy eigenvalue matrix. Accordingly, the time-periodic part of the wave function is unitary transformed as follows:

$$|\psi(\mathbf{k})\rangle = \hat{\mathcal{U}}(\mathbf{k})|\tilde{\psi}(\mathbf{k})\rangle, \tag{A6}$$

where $|\tilde{\psi}(\mathbf{k})\rangle$ is the time-periodic part of the wave function expressed in terms of the instantaneous eigenstate basis.

As a consequence of the above unitary transformation, $|\tilde{\psi}(\mathbf{k})\rangle$ now satisfies the following equation:

$$\epsilon|\tilde{\psi}(\mathbf{k})\rangle = \left(\hat{\mathcal{E}}(\mathbf{k}) + \Omega\left[i\frac{\partial}{\partial\kappa} + i\hat{\mathcal{U}}^\dagger(\mathbf{k})\frac{\partial}{\partial\kappa}\hat{\mathcal{U}}(\mathbf{k})\right]\right)|\tilde{\psi}(\mathbf{k})\rangle. \tag{A7}$$

The last step for the derivation of the TSH is to note that the second term in the bracket is actually the very definition of the Berry connection:

$$\hat{\mathcal{A}}_\kappa(\mathbf{k}) = i\hat{\mathcal{U}}^\dagger(\mathbf{k})\frac{\partial}{\partial\kappa}\hat{\mathcal{U}}(\mathbf{k}). \tag{A8}$$

Finally, the TSH is defined such that its diagonalization gives rise to the quasienergy,

$$\epsilon|\tilde{\psi}(\mathbf{k})\rangle = \hat{H}_{\rm TS}(\mathbf{k})|\tilde{\psi}(\mathbf{k})\rangle, \tag{A9}$$

where

$$\hat{H}_{\rm TS}(\mathbf{k}) = \hat{\mathcal{E}}(\mathbf{k}) + \Omega\left[i\frac{\partial}{\partial\kappa} + \hat{\mathcal{A}}_\kappa(\mathbf{k})\right]. \tag{A10}$$

APPENDIX B: HIGH-FREQUENCY EFFECTIVE HAMILTONIAN OF IRRADIATED GRAPHENE

In the limit of high frequency, the TSH can be expanded up to the order of $1/\Omega$ as follows:

$$\mathcal{H}_{{\rm eff},\nu} = \nu\Omega\hat{I} + \mathbf{d}_{\mathbf{k}_\perp}\cdot\boldsymbol{\sigma}, \tag{B1}$$

describing the effective dynamics of the νth pair of the quasienergy band. For convenience, let us rewrite the results obtained in Eq. (12):

$$d_{\mathbf{k}_\perp,+} = d_{\mathbf{k}_\perp,x} + id_{\mathbf{k}_\perp,y} = \Gamma_0^*(\mathbf{k}_\perp), \tag{B2}$$

$$d_{\mathbf{k}_\perp,-} = d_{\mathbf{k}_\perp,x} - id_{\mathbf{k}_\perp,y} = \Gamma_0(\mathbf{k}_\perp), \tag{B3}$$

$$d_{\mathbf{k}_\perp,z} = \sum_{n=1}^{\infty}\frac{|\Gamma_n(\mathbf{k}_\perp)|^2 - |\Gamma_{-n}(\mathbf{k}_\perp)|^2}{n\Omega}, \tag{B4}$$

where

$$\Gamma_n(\mathbf{k}_\perp) = e^{i\phi_0(\mathbf{k}_\perp)}\int_0^{2\pi}\frac{d\kappa}{2\pi}g_{\mathbf{k}}e^{in\kappa}, \tag{B5}$$

with $\phi_0(\mathbf{k}_\perp) = \phi(\mathbf{k}_\perp, \kappa = 0)$.

In the nearest-neighbor tight-binding model of graphene,

$$g_{\mathbf{k}} = -\tau\sum_{j=1}^{3}e^{i\mathbf{k}_\perp^{\rm Pei-sub}\cdot\mathbf{c}_j}, \tag{B6}$$

where $\mathbf{k}_\perp^{\rm Pei-sub} = (k_x - A\cos\kappa, k_y - A\sin\kappa)$ with $\mathbf{c}_1 = (-\sqrt{3}/2, -1/2)$, $\mathbf{c}_2 = (\sqrt{3}/2, -1/2)$, and $\mathbf{c}_3 = (0, 1)$ in units of lattice spacing, which is set to be unity. After some algebra, one can show that

$$g_{\mathbf{k}} = -\tau\sum_{j=1}^{3}e^{i\mathbf{k}_\perp\cdot\mathbf{c}_j}e^{-iA\cos(\kappa-\theta_j)}, \tag{B7}$$

where $\cos\theta_j = \mathbf{c}_{j,x}$ and $\sin\theta_j = \mathbf{c}_{j,y}$. Then, Eq. (B5) can be rewritten as follows:

$$\begin{aligned}\frac{\Gamma_n(\mathbf{k}_\perp)}{e^{i\phi_0(\mathbf{k}_\perp)}} &= -\tau\sum_{j=1}^{3}e^{i\mathbf{k}_\perp\cdot\mathbf{c}_j}\int_0^{2\pi}\frac{d\kappa}{2\pi}e^{in\kappa}e^{-iA\cos(\kappa-\theta_j)}\\ &= -\tau i^n J_n(-A)\sum_j e^{i\mathbf{k}_\perp\cdot\mathbf{c}_j}e^{in\theta_j},\end{aligned} \tag{B8}$$

where the definition of the Bessel function has been used: $J_n(z) = \int\frac{d\phi}{2\pi i^n}e^{in\phi}e^{iz\cos\phi}$.

We are interested in the modulus square of $\Gamma_n(\mathbf{k}_\perp)$ for $n \neq 0$:

$$|\Gamma_n(\mathbf{k}_\perp)|^2 = \tau^2 J_n^2(A)\left|\sum_{j=1}^{3}e^{i\mathbf{k}_\perp\cdot\mathbf{c}_j}e^{in\theta_j}\right|^2. \tag{B9}$$

Meanwhile, for $n = 0$, $\Gamma_0(\mathbf{k}_\perp)$ itself is important,

$$\Gamma_0(\mathbf{k}_\perp) = -\tau J_0(A)e^{i\phi_0(\mathbf{k}_\perp)}\sum_{j=1}^{3}e^{i\mathbf{k}_\perp\cdot\mathbf{c}_j}, \tag{B10}$$

where we have used $J_n(-z) = (-1)^n J_n(z)$. By using these expressions, one can rewrite Eq. (B4) as follows:

$$d_{\mathbf{k}_\perp,z} = \frac{\tau^2}{\Omega}\sum_{n=1}^{\infty}\frac{J_n^2(A)}{n}\mathcal{F}_n(\mathbf{k}_\perp), \tag{B11}$$

where we have used $J_{-n}(z) = (-1)^n J_n(z)$ and

$$\begin{aligned}\mathcal{F}_n(\mathbf{k}_\perp) &= \left|\sum_{j=1}^{3}e^{i\mathbf{k}_\perp\cdot\mathbf{c}_j}e^{in\theta_j}\right|^2 - \left|\sum_{j=1}^{3}e^{i\mathbf{k}_\perp\cdot\mathbf{c}_j}e^{-in\theta_j}\right|^2\\ &= 2i\sum_{j\neq k}\sin(n\theta_{jk})e^{i\mathbf{k}_\perp\cdot\mathbf{c}_{jk}},\end{aligned} \tag{B12}$$

where $\theta_{jk} = \theta_j - \theta_k$ and $\mathbf{c}_{jk} = \mathbf{c}_j - \mathbf{c}_k$. Now, it is important to note that $\mathbf{c}_{jk}$ are actually the displacement vectors connecting between next-nearest-neighboring sites in graphene. That is, there are six displacement vectors: $\boldsymbol{\eta}_1 = \mathbf{c}_{13}$, $\boldsymbol{\eta}_2 = \mathbf{c}_{23}$, $\boldsymbol{\eta}_3 = \mathbf{c}_{21}$, $\boldsymbol{\eta}_4 = \mathbf{c}_{31}$, $\boldsymbol{\eta}_5 = \mathbf{c}_{32}$, and $\boldsymbol{\eta}_6 = \mathbf{c}_{12}$. Also noting that $\theta_{12} = \theta_{23} = \theta_{31} = -\theta_{21} = -\theta_{32} = -\theta_{13} = -2\pi/3$, one can rewrite Eq. (B12) as follows:

$$\mathcal{F}_n(\mathbf{k}_\perp) = 2i\sin\left(\frac{2n\pi}{3}\right)\sum_{j=1}^{6}(-1)^j e^{i\mathbf{k}_\perp\cdot\boldsymbol{\eta}_j}. \tag{B13}$$

Finally, after collecting all the factors, $d_{\mathbf{k}_\perp,z}$ can be written as

$$d_{\mathbf{k}_\perp,z} = i\lambda_{\rm eff}(A)\sum_{j=1}^{6}(-1)^j e^{i\mathbf{k}_\perp\cdot\boldsymbol{\eta}_j}, \tag{B14}$$

where

$$\frac{\lambda_{\rm eff}(A)}{\tau^2/\Omega} = 2\sum_{n=1}^{\infty}\frac{J_n^2(A)}{n}\sin\left(\frac{2n\pi}{3}\right). \tag{B15}$$

Also, by using Eq. (B10), $d_{\mathbf{k}_\perp,\pm}$ can be written as

$$d_{\mathbf{k}_\perp,+}^* = d_{\mathbf{k}_\perp,-} = -\tau_{\rm eff}(A)e^{i\phi_0(\mathbf{k}_\perp)}\sum_{j=1}^{3}e^{i\mathbf{k}_\perp\cdot\mathbf{c}_j}, \tag{B16}$$

where $\tau_{\rm eff}(A) = \tau J_0(A)$. Note that the phase factor $e^{i\phi_0(\mathbf{k}_\perp)}$ is not important since it can be removed via an appropriate gauge transformation.

APPENDIX C: QUASIENERGY GAP NEAR THE PROJECTED HELICAL NODAL LINE AT LOW FREQUENCY

The quasienergy gap opens up when two different time WSL eigenstates with one from the conduction band and the

other from the valence band are mixed together. The mixing matrix element between these two time WSL eigenstates is given by

$$\mathcal{M}_{nn'}(\mathbf{k}_\perp) = \frac{\Omega}{2}\int_0^{2\pi}\frac{d\kappa}{2\pi}\left[\psi^{\mathrm{WSL}}_{+,n}(\mathbf{k})\right]^*\frac{\partial\phi(\mathbf{k})}{\partial\kappa}\psi^{\mathrm{WSL}}_{-,n'}(\mathbf{k}), \quad \text{(C1)}$$

since $\mathcal{A}^{\pm\mp}_\kappa(\mathbf{k}) = \frac{1}{2}\frac{\partial}{\partial\kappa}\phi(\mathbf{k})$. Also,

$$\psi^{\mathrm{WSL}}_{\pm,n}(\mathbf{k}) = e^{-\frac{i}{\Omega}\int_0^\kappa d\kappa'\left[\mathcal{E}^{\mathrm{WSL}}_{\pm,n}(\mathbf{k}_\perp)-\epsilon_\pm(\mathbf{k}')-\frac{\Omega}{2}\frac{\partial}{\partial\kappa}\phi(\mathbf{k}')\right]}, \quad \text{(C2)}$$

since $\mathcal{A}^{\pm\pm}_\kappa(\mathbf{k}) = \frac{1}{2}\frac{\partial}{\partial\kappa}\phi(\mathbf{k})$.

Now, due to the convenient fact that all the terms depending on the Zak phase cancel each other completely, the mixing matrix element can be written in a single formula regardless of whether $\mathbf{k}_\perp$ is located inside or outside the projected helical nodal line:

$$\mathcal{M}_{nn'}(\mathbf{k}_\perp) = \frac{\Omega}{2}\int_0^{2\pi}\frac{d\kappa}{2\pi}\frac{\partial\phi(\mathbf{k})}{\partial\kappa}e^{-i\Delta n\kappa}e^{\frac{i}{\Omega}\int_0^\kappa d\kappa'[\Delta\epsilon(\mathbf{k}')-\Delta\bar{\epsilon}]}, \quad \text{(C3)}$$

where $\Delta n = n - n'$, $\Delta\epsilon(\mathbf{k}) = \epsilon_+(\mathbf{k}) - \epsilon_-(\mathbf{k})$, and $\Delta\bar{\epsilon} = \bar{\epsilon}_+(\mathbf{k}_\perp) - \bar{\epsilon}_-(\mathbf{k}_\perp)$. By inspecting the form of the above integral, one can find that the most important contribution comes from the region, where $\phi(\mathbf{k})$ changes significantly as a function of κ.

It can be shown from Eq. (5) that $\phi(\mathbf{k})$ changes significantly around the critical value of κ, $\kappa_c(\mathbf{k}_\perp)$, where the helical nodal line is the closest to the constant $\mathbf{k}_\perp$ line. For convenience, let us define $f(\kappa) = \frac{\partial}{\partial\kappa}\phi(\mathbf{k})$, which is written as a function of κ with the $\mathbf{k}_\perp$ dependence being implicit. Now, one can expand $f(\kappa)$ around κ_c; $f(\kappa) \simeq f_c + f'_c\Delta\kappa + \frac{f''_c}{2}(\Delta\kappa)^2$, where $f_c = f(\kappa=\kappa_c)$, $f'_c = f'(\kappa=\kappa_c)$, $f''_c = f''(\kappa=\kappa_c)$, and $\Delta\kappa = \kappa - \kappa_c$. Since $f'_c = 0$ due to the very definition of κ_c, one can approximate $f(\kappa)$ as follows:

$$f(\kappa) \simeq f_c e^{\frac{f''_c}{2f_c}(\Delta\kappa)^2}. \quad \text{(C4)}$$

Under this expansion scheme, one can then rewrite Eq. (C3) as follows:

$$\frac{\mathcal{M}_{nn'}}{\Omega f_c/2} \simeq \int_0^{2\pi}\frac{d\kappa}{2\pi}e^{\frac{f''_c}{2f_c}(\Delta\kappa)^2}e^{-i\Delta n\kappa}e^{\frac{i}{\Omega}\int_0^\kappa d\kappa'[\Delta\epsilon(\mathbf{k}')-\Delta\bar{\epsilon}]}. \quad \text{(C5)}$$

Note that the $\mathbf{k}_\perp$ dependence is not explicitly written from this forward unless it is necessary.

In the limit of low frequency, the last exponential term in Eq. (C5) fluctuates wildly unless its argument is nearly zero. To take care of this wildly fluctuating term, let us first rewrite Eq. (C5) as follows:

$$\frac{\mathcal{M}_{nn'}}{\Omega f_c/2} \simeq \mathcal{C}\int_0^{2\pi}\frac{d\kappa}{2\pi}e^{\frac{f''_c}{2f_c}(\Delta\kappa)^2}e^{-i\Delta n\Delta\kappa}e^{\frac{i}{\Omega}\int_{\kappa_c}^\kappa d\kappa'[\Delta\epsilon(\mathbf{k}')-\Delta\bar{\epsilon}]}, \quad \text{(C6)}$$

where $\mathcal{C} = e^{-i\Delta n\kappa_c}e^{\frac{i}{\Omega}\int_0^{\kappa_c}d\kappa'[\Delta\epsilon(\mathbf{k}')-\Delta\bar{\epsilon}]}$ is just a constant phase factor. Then, we expand the argument of the last exponential term up to the linear of order of $\Delta\kappa$ as follows:

$$\frac{\mathcal{M}_{nn'}}{\Omega f_c/2} \simeq \mathcal{C}\int_0^{2\pi}\frac{d\kappa}{2\pi}e^{\frac{f''_c}{2f_c}(\Delta\kappa)^2}e^{-i\left[\Delta n-\frac{1}{\Omega}(\Delta\epsilon_c-\Delta\bar{\epsilon})\right]\Delta\kappa}, \quad \text{(C7)}$$

where $\Delta\epsilon_c = \Delta\epsilon(\mathbf{k}_\perp, \kappa=\kappa_c)$.

Then, as a final approximation, we take the upper and lower limits of the integral to be plus and minus infinity and perform the Gaussian integration with respect to $\Delta\kappa$:

$$\frac{\mathcal{M}_{nn'}}{\Omega f_c/2} \simeq \mathcal{C}\int_{-\infty}^{\infty}\frac{d\kappa}{2\pi}e^{-\alpha(\Delta\kappa)^2}e^{i\beta\Delta\kappa} = \frac{\mathcal{C}}{2\pi}\sqrt{\frac{\pi}{\alpha}}e^{-\frac{\beta^2}{4\alpha}}, \quad \text{(C8)}$$

where $\alpha = -f''_c/2f_c$ and $\beta = \frac{1}{\Omega}(\Delta\epsilon_c - \Delta\bar{\epsilon}) - \Delta n$. Note that the above Gaussian integration is valid since $\alpha > 0$ as shown by an explicit calculation.

We are interested in the quasienergy gap at zero quasienergy, or any other quasienergy value where the quasienergy of the time WSL eigenstate from the conduction band matches exactly that from the valence band. Mathematically, this means that $\Delta\bar{\epsilon} + \Omega\Delta n = 0$. In other words, the diagonal matrix element is exactly the same for both of the time WSL eigenstates from the conduction and valence bands. In this situation, the quasienergy gap is given simply by twice the absolute value of the mixing matrix element:

$$\mathcal{E}_{\mathrm{gap}} = 2|\mathcal{M}_{\Delta n=-\Delta\bar{\epsilon}/\Omega}| \simeq \frac{\Omega f_c}{2\pi}\sqrt{\frac{\pi}{\alpha}}e^{-\frac{(\Delta\epsilon_c)^2}{4\alpha\Omega^2}}. \quad \text{(C9)}$$

Finally, in the continuum limit, the graphene Hamiltonian is taken to be linear in the vicinity of a given Dirac node, i.e., $g_{\mathbf{q}} = \tau[(q_x - A\cos\kappa) + i(q_y - A\sin\kappa)]$, where $\mathbf{q}_\perp = (q_x, q_y) = \mathbf{k}_\perp - \mathbf{K}_{\mathrm{Dirac}}$ is the momentum measured from the Dirac node. Here, $f(\kappa) = \frac{\partial}{\partial\kappa}\phi(q_x, q_y, \kappa)$ can be obtained analytically,

$$f(\kappa) = \frac{1 - \frac{\rho}{A}\cos(\kappa-\theta)}{1 - \left(\frac{\rho}{A}\right)^2 - 2\frac{\rho}{A}\cos(\kappa-\theta)}, \quad \text{(C10)}$$

where $\rho = \sqrt{q_x^2 + q_y^2}$ and $\tan\theta = q_y/q_x$. The above formula can be derived by noting that $g_{\mathbf{q}} = \rho e^{i\theta} - Ae^{i\kappa}$. By using this formula, one can determine $f_c = \frac{A}{A-\rho}$ and $\alpha = \frac{\rho(A+\rho)}{2(A-\rho)^2}$ with $\kappa_c = \theta$. Also, one can show $\Delta\epsilon_c = 2|g_{(\mathbf{q}_\perp,\kappa_c)}| = 2\tau|A-\rho|$ in the continuum limit. Inserting f_c, α, and $\Delta\epsilon_c$ into Eq. (C9), we arrive at the following formula for the quasienergy gap in the continuum limit:

$$\mathcal{E}_{\mathrm{gap}} \simeq \frac{\Omega A}{\sqrt{2\pi\rho(A+\rho)}}e^{-\frac{2(A-\rho)^4}{\rho(A+\rho)(\Omega/\tau)^2}}. \quad \text{(C11)}$$

It is important to note that, due to the exponential suppression term, the quasienergy gap near the projected helical nodal line vanishes much faster than Ω as soon as ρ becomes separated from A by roughly more than $\sqrt{A\Omega/\tau}$. Consequently, in the limit of low frequency, the time WSL eigenstates become more and more sharply defined with the correspondingly pronounced topological discontinuity across the projected helical nodal line.

APPENDIX D: ABELIAN WEIGHT OF THE FULL FLOQUET STATES

Here, we provide some details on how to compute the Abelian weight of the full Floquet states obtained by

diagonalizing the Floquet Hamiltonian. In other words, we would like to decompose the full Floquet states, $|\psi_\alpha(\mathbf{k})\rangle$, in terms of the conduction/valence time WSL eigenstates, $\psi^{\rm WSL}_{\pm,n}(\mathbf{k})$, obtained by ignoring the off-diagonal elements of the Berry connection. Mathematically, the Abelian weight of the αth full Floquet states is defined as follows:

$$\mathcal{W}_{\pm,\alpha}(\mathbf{k}_\perp) = \sum_n \left| \int_0^{2\pi} \frac{d\kappa}{2\pi} \psi^*_{\pm,\alpha}(\mathbf{k}) \psi^{\rm WSL}_{\pm,n}(\mathbf{k}) \right|^2 = \int_0^{2\pi} \frac{d\kappa}{2\pi} |\psi_{\pm,\alpha}(\mathbf{k})|^2, \tag{D1}$$

where $\psi_{\pm,\alpha}(\mathbf{k})$ is the $\pm$, or conduction/valence component of $|\psi_\alpha(\mathbf{k})\rangle$. The second line is obtained due to the completeness of the time WSL eigenstates. Also, $\mathcal{W}_{+,\alpha} + \mathcal{W}_{-,\alpha} = 1$ due to the normalization of the Floquet states. Therefore, the Abelian weight is nothing but the projection weight of the full Floquet states onto the instantaneous eigenstate basis.

Now, suppose that one obtains the full Floquet states by diagonalizing the Floquet Hamiltonian $\hat{H}_{\rm F}$ expressed in terms of the Floquet and sublattice index, not the TSH expressed in terms of time and the instantaneous energy eigenvalue index. That is,

$$|\psi_\alpha(\mathbf{k})\rangle = \sum_m e^{-im\kappa} \begin{pmatrix} a_{\alpha,m}(\mathbf{k}_\perp) \\ b_{\alpha,m}(\mathbf{k}_\perp) \end{pmatrix}, \tag{D2}$$

where $a_{\alpha,m}$ and $b_{\alpha,m}$ denote the amplitude of the Floquet state in each sublattice basis. To compute the Abelian weight in terms of this representation, one needs to perform a unitary transformation of this Floquet state to the instantaneous eigenstate basis. Mathematically,

$$\psi_{\pm,\alpha}(\mathbf{k}) = \langle \pm | U^\dagger(\mathbf{k}) | \psi_\alpha(\mathbf{k}) \rangle, \tag{D3}$$

where $\langle \pm| = (1, 0)$ and (0,1), respectively. The unitary transformation matrix is given by

$$U(\mathbf{k}) = \frac{1}{\sqrt{2}} \begin{pmatrix} e^{-i\phi(\mathbf{k})} & e^{-i\phi(\mathbf{k})} \\ 1 & -1 \end{pmatrix} = \frac{1}{\sqrt{2}} \sum_n e^{-in\kappa} \begin{pmatrix} \varphi_n(\mathbf{k}_\perp) & \varphi_n(\mathbf{k}_\perp) \\ \delta_{n,0} & -\delta_{n,0} \end{pmatrix}, \tag{D4}$$

where $\varphi_n(\mathbf{k}_\perp)$ is the nth time-conjugate Fourier component of $e^{-i\phi(\mathbf{k})}$. Then, after plugging all the above expressions into Eq. (D1) and performing the time integration, one can obtain the following result:

$$\mathcal{W}_{\pm,\alpha} = \frac{1}{2} \pm \sum_{n,m} \mathrm{Re}(\varphi_n a^*_{\alpha,m} b_{\alpha,m-n}), \tag{D5}$$

where the $\mathbf{k}_\perp$ argument is not explicitly written for simplicity.

[1] F. D. M. Haldane, Model for a Quantum Hall Effect Without Landau levels: Condensed-Matter Realization of the "Parity Anomaly," Phys. Rev. Lett. **61**, 2015 (1988).

[2] C. L. Kane and E. J. Mele, Quantum Spin Hall Effect in Graphene, Phys. Rev. Lett. **95**, 226801 (2005).

[3] M. König, S. Wiedmann, C. Brüne, A. Roth, H. Buhmann, L. W. Molenkamp, X.-L. Qi, and S.-C. Zhang, Quantum spin Hall insulator state in HgTe quantum wells, Science **318**, 766 (2007).

[4] M. Z. Hasan and C. L. Kane, Colloquium: Topological insulators, Rev. Mod. Phys. **82**, 3045 (2010).

[5] X.-L. Qi and S.-C. Zhang, Topological insulators and superconductors, Rev. Mod. Phys. **83**, 1057 (2011).

[6] K. Park, A passage to topological matter: Colloquium, J. Korean Phys. Soc. **73**, 817 (2018).

[7] S. Murakami, Phase transition between the quantum spin Hall and insulator phases in 3D: Emergence of a topological gapless phase, New J. Phys. **9**, 356 (2007).

[8] X. Wan, A. M. Turner, A. Vishwanath, and S. Y. Savrasov, Topological semimetal and Fermi-arc surface states in the electronic structure of pyrochlore iridates, Phys. Rev. B **83**, 205101 (2011).

[9] Z. Wang, Y. Sun, X.-Q. Chen, C. Franchini, G. Xu, H. Weng, X. Dai, and Z. Fang, Dirac Semimetal and Topological Phase Transitions in A_3Bi (A = Na, K, Rb), Phys. Rev. Lett. **85**, 195320 (2012).

[10] A. A. Burkov, M. D. Hook, and L. Balents, Topological nodal semimetals, Phys. Rev. B **84**, 235126 (2011).

[11] G. Xu, H. Weng, Z. Wang, X. Dai, and Z. Fang, Chern Semimetal and the Quantized Anomalous Hall Effect in $HgCr_2Se_4$, Phys. Rev. Lett. **107**, 186806 (2011).

[12] J.-M. Carter, V. V. Shankar, M. A. Zeb, and H.-Y. Kee, Semimetal and topological insulator in perovskite iridates, Phys. Rev. B **85**, 115105 (2012).

[13] H. Weng, Y. Liang, Q. Xu, R. Yu, Z. Fang, X. Dai, and Y. Kawazoe, Topological nodal-line semimetal in three-dimensional graphene networks, Phys. Rev. B **92**, 045108 (2015).

[14] C. Fang, Y. Chen, H.-Y. Kee, and L. Fu, Topological nodal line semimetals with and without spin-orbital coupling, Phys. Rev. B **92**, 081201(R) (2015).

[15] Y. Kim, B. J. Wieder, C. L. Kane, and A. M. Rappe, Dirac line Nodes in Inversion-Symmetric Crystals, Phys. Rev. Lett. **115**, 036806 (2015).

[16] R. Yu, H. Weng, Z. Fang, X. Dai, and X. Hu, Topological Nodal-Line Semimetal and Dirac Semimetal State in Antiperovskite Cu_3PdN, Phys. Rev. Lett. **115**, 036807 (2015).

[17] L. S. Xie, L. M. Schoop, E. M. Seibel, Q. D. Gibson, W. Xie, and R. J. Cava, A new form of Ca_3P_2 with a ring of Dirac nodes, APL Mater. **3**, 083602 (2015).

[18] Y. Chen, Y. Xie, S. A. Yang, H. Pan, F. Zhang, M. Cohen, and S. Zhang, Nanostructured carbon allotropes with Weyl-like loops and points, Nano Lett. **15**, 6974 (2015).

[19] Q.-F. Liang, J. Zhou, R. Yu, Z. Wang, and H. Weng, Nodal-surface and nodal-line fermions from nonsymmorphic lattice symmetries, Phys. Rev. B **93**, 085427 (2016).

[20] H. Huang, J. Liu, D. Vanderbilt, and W. Duan, Topological nodal-line semimetals in alkaline-earth stannides, germanides, and silicides, Phys. Rev. B **93**, 201114(R) (2016).

[21] Y.-H. Chan, C.-K. Chiu, M. Y. Chou, and A. P. Schnyder, Ca_3P_2 and other topological semimetals with line nodes and drumhead surface states, Phys. Rev. B **93**, 205132 (2016).

[22] A. Yamakage, Y. Yamakawa, Y. Tanaka, and Y. Okamoto, Line-node Dirac semimetal and topological insulating phase in noncentrosymmetric pnictides CaAgX ($X = P$, As), J. Phys. Soc. Jpn. **85**, 013708 (2016).

[23] T. Oka and S. Kitamura, Floquet engineering of quantum materials, Annu. Rev. Condens. Matter Phys. **10**, 387 (2019).

[24] T. Oka and H. Aoki, Photovoltaic Hall effect in graphene, Phys. Rev. B **79**, 081406(R) (2009).

[25] T. Kitagawa, T. Oka, A. Brataas, L. Fu, and E. Demler, Transport properties of nonequilibrium systems under the application of light: Photoinduced quantum Hall insulators with Landau levels, Phys. Rev. B **84**, 235108 (2011).

[26] A. Kundu, H. A. Fertig, and B. Seradjeh, Effective Theory of Floquet Topological Transitions, Phys. Rev. Lett. **113**, 236803 (2014).

[27] H. Dehghani, T. Oka, and A. Mitra, Out-of-equilibrium electrons and the Hall conductance of a Floquet topological insulator, Phys. Rev. B **91**, 155422 (2015).

[28] M. A. Sentef, M. Claassen, A. F. Kemper, B. Moritz, T. Oka, J. K. Freericks, and T. P. Devereaux, Theory of Floquet band formation and local pseudospin textures in pump-probe photoemission of graphene, Nat. Commun. **6**, 7047 (2015).

[29] T. Mikami, S. Kitamura, K. Yasuda, N. Tsuji, T. Oka, and H. Aoki, Brillouin-Wigner theory for high-frequency expansion in periodically driven systems: Application to Floquet topological insulators, Phys. Rev. B **93**, 144307 (2016).

[30] N. H. Lindner, G. Refael, and V. Galitski, Floquet topological insulator in semiconductor quantum wells, Nat. Phys. **7**, 490 (2011).

[31] Y. H. Wang, H. Steinberg, P. Jarillo-Herrero, and N. Gedik, Observation of Floquet-Bloch states on the surface of a topological insulator, Science **342**, 453 (2013).

[32] F. Mahmood, C.-K. Chan, Z. Alpichshev, D. Gardner, Y. Lee, P. A. Lee, and N. Gedik, Selective scattering between Floquet-Bloch and Volkov states in a topological insulator, Nat. Phys. **12**, 306 (2016).

[33] A. Gómez-León and G. Platero, Floquet-Bloch theory and Topology in Periodically Driven Lattices, Phys. Rev. Lett. **110**, 200403 (2013).

[34] W.-R. Lee and K. Park, Direct manifestation of topological order in the winding number of the Wannier-Stark ladder, Phys. Rev. B **92**, 195144 (2015).

[35] K. W. Kim, W.-R. Lee, Y. B. Kim, and K. Park, Surface to bulk Fermi arcs via Weyl nodes as topological defects, Nat. Commun. **7**, 13489 (2016).

[36] A. Eckardt and E. Anisimovas, High-frequency approximation for periodically driven quantum systems from a Floquet-space perspective, New J. Phys. **17**, 093039 (2015).

[37] J. W. McIver, B. Schulte, F.-U. Stein, T. Matsuyama, G. Jotzu, G. Meier, and A. Cavalleri, Light-induced anomalous Hall effect in graphene, arXiv:1811.03522.

[38] F. Casas, J. A. Oteo, and J. Ros, Floquet theory: Exponential perturbative treatment, J. Phys. A: Math. Gen. **34**, 3379 (2001).

[39] S. Rahav, I. Gilary, and S. Fishman, Effective Hamiltonians for periodically driven systems, Phys. Rev. A **68**, 013820 (2003).

[40] E. S. Mananga and T. Charpentier, Introduction of the Floquet-Magnus expansion in solid-state nuclear magnetic resonance spectroscopy, J. Chem. Phys. **135**, 044109 (2011).

[41] H. K. Kelardeh, V. Apalkov, and M. I. Stockman, Attosecond strong-field interferometry in graphene: Chirality, singularity, and the Berry phase, Phys. Rev. B **93**, 155434 (2016).

[42] H. K. Kelardeh, V. Apalkov, and M. I. Stockman, Graphene superlattices in strong circularly polarized fields: Chirality, Berry phase, and attosecond dynamics, Phys. Rev. B **96**, 075409 (2017).

[43] W. P. Su, J. R. Schrieffer, and A. J. Heeger, Soliton excitations in polyacetylene, Phys. Rev. B **22**, 2099 (1980).

[44] J. Zak, Berry's Phase for Energy Bands in Solids, Phys. Rev. Lett. **62**, 2747 (1989).

[45] R. D. King-Smith and D. Vanderbilt, Theory of polarization of crystalline solids, Phys. Rev. B **47**, 1651 (1993).

[46] P. Delplace, D. Ullmo, and G. Montambaux, Zak phase and the existence of edge states in graphene, Phys. Rev. B **84**, 195452 (2011).

[47] G. Rigolin, G. Ortiz, and V. H. Ponce, Beyond the quantum adiabatic approximation: adiabatic perturbation theory, Phys. Rev. A **78**, 052508 (2008).

[48] H. Martiskainen and N. Moiseyev, Perturbation theory for quasienergy Floquet solutions in the low-frequency regime of the oscillating electric field, Phys. Rev. A **91**, 023416 (2015).

[49] M. Rodriguez-Vega, M. Lentz, and B. Seradjeh, Floquet perturbation theory: Formalism and application to low-frequency limit, New J. Phys. **20**, 093022 (2018).